Volume 18
Number 3
21 January 2022
Pages 467–688

Soft Matter

rsc.li/soft-matter-journal

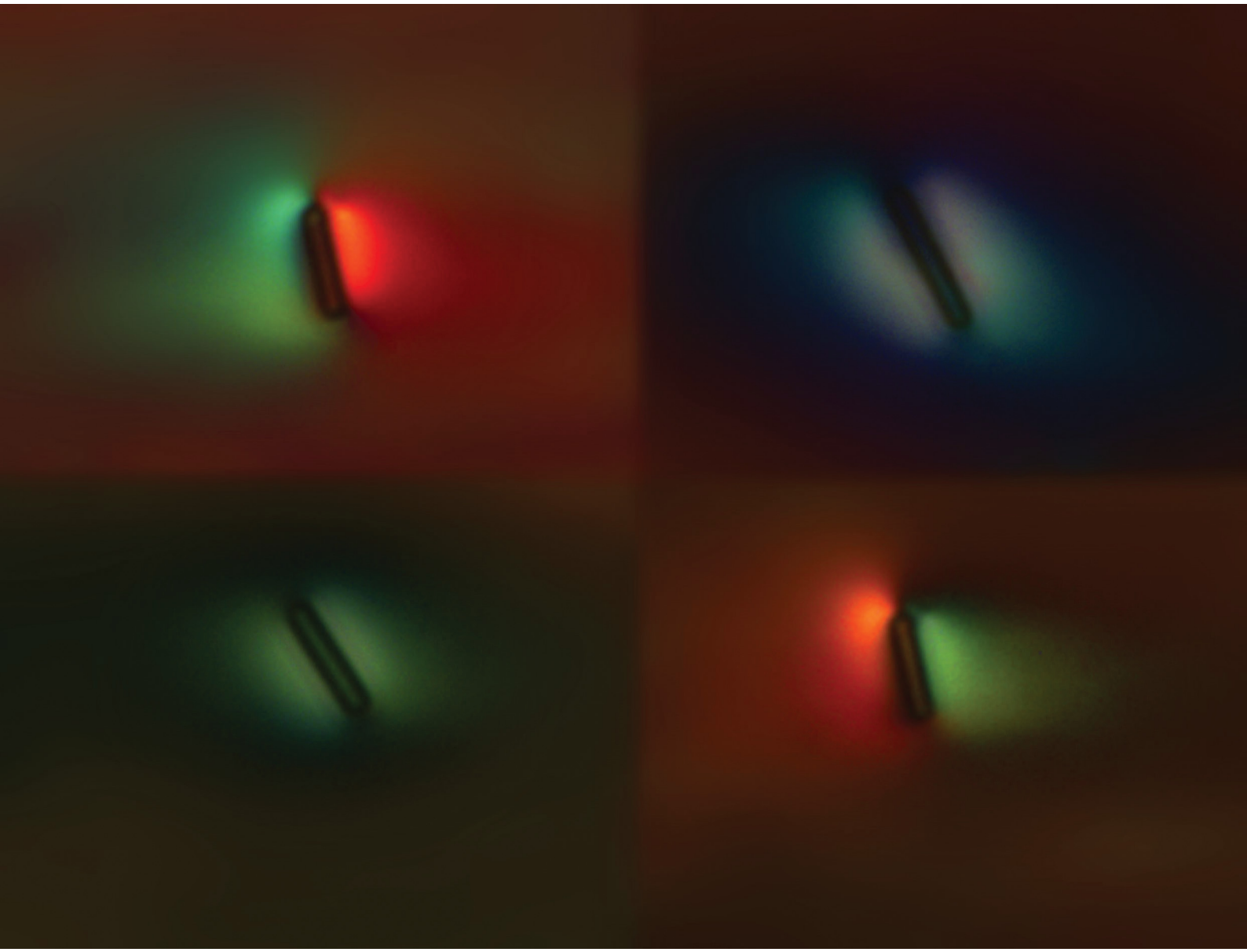

ISSN 1744-6848

ROYAL SOCIETY OF CHEMISTRY

PAPER

Sophie Ettinger *et al.*

Rods in a lyotropic chromonic liquid crystal: emergence of chirality, symmetry-breaking alignment, and caged angular diffusion

Soft Matter

PAPER

View Article Online
View Journal | View Issue

Cite this: *Soft Matter*, 2022, **18**, 487

Rods in a lyotropic chromonic liquid crystal: emergence of chirality, symmetry-breaking alignment, and caged angular diffusion†

Sophie Ettinger, *[a] Clarissa F. Dietrich,[b] Chandan K. Mishra,[c] Cornelia Miksch,[d] Daniel A. Beller,[e] Peter J. Collings[af] and A. G. Yodh[a]

Received 17th August 2021,
Accepted 19th November 2021

DOI: 10.1039/d1sm01209f

rsc.li/soft-matter-journal

In lyotropic chromonic liquid crystals (LCLCs), twist distortion of the nematic director costs much less energy than splay or bend distortion. This feature leads to novel mirror-symmetry breaking director configurations when the LCLCs are confined by interfaces or contain suspended particles. Spherical colloids in an aligned LCLC nematic phase, for example, induce chiral director perturbations ("twisted tails"). The asymmetry of rod-like particles in an aligned LCLC offer a richer set of possibilities due to their aspect ratio (α) and mean orientation angle ($\langle\theta\rangle$) between their long axis and the uniform far-field director. Here we report on the director configuration, equilibrium orientation, and angular diffusion of rod-like particles with planar anchoring suspended in an aligned LCLC. Video microscopy reveals, counterintuitively, that two-thirds of the rods have an angled equilibrium orientation ($\langle\theta\rangle \neq 0$) that decreases with increasing α, while only one-third of the rods are aligned ($\langle\theta\rangle = 0$). Polarized optical video-microscopy and Landau–de Gennes numerical modeling demonstrate that the angled and aligned rods are accompanied by distinct chiral director configurations. Angled rods have a longitudinal mirror plane (LMP) parallel to their long axis and approximately parallel to the substrate walls. Aligned rods have a transverse and longitudinal mirror plane (TLMP), where the transverse mirror plane is perpendicular to the rod's long axis. Effectively, the small twist elastic constant of LCLCs promotes chiral director configurations that modify the natural tendency of rods to orient along the far-field director. Additional diffusion experiments confirm that rods are angularly confined with strength that depends on α.

1 Introduction

Nematic phases form in thermotropic and lyotropic chromonic liquid crystals (LCLCs) and exhibit many similar properties. The elastic behavior of both types of liquid crystals (LCs) is governed by splay, twist, and bend director distortions, each with material-specific elastic constants. The twist elastic constant in LCLCs, however, is approximately one order of magnitude smaller than their splay and bend elastic constants.[1] In thermotropic LCs, the three constants are comparable.[2–5] The large difference in twist elasticity has a surprising consequence; it produces mirror-symmetry breaking director configurations in LCLCs, but rarely in thermotropic nematic LCs.[6–9] These chiral director perturbations arise when LCLCs are confined within spheres,[10] cylinders,[11–15] and tactoids,[16,17] and similar chiral distortions occur around particles suspended in LCLCs.[18,19] The latter director configurations and their consequences have been studied in only one context: spherical colloidal particles with planar anchoring in an aligned nematic LCLC. Interestingly, mirror symmetry-breaking chiral director perturbations form around the spheres ("twisted tails"), although neither the liquid crystal nor the particles are inherently chiral.[18,19]

Here we study suspended rod-like particles in an aligned LCLC nematic phase. Previously, theoretical and experimental studies of the orientation and diffusion of rods in aligned nematic LCs have largely focused on rods with perpendicular surface anchoring,[20–23] since rods with planar anchoring are expected to align parallel to the uniform far-field director with little disturbance to the local director.[21,24,25] To the best of our

[a] *Department of Physics and Astronomy, University of Pennsylvania, Philadelphia, PA, 19104, USA. E-mail: asophie@sas.upenn.edu*
[b] *Institute of Physical Chemistry, University of Stuttgart, Pfaffenwaldring 55, 70569 Stuttgart, Germany*
[c] *Discipline of Physics, Indian Institute of Technology (IIT) Gandhinagar, Palaj, Gandhinagar, Gujarat 382355, India*
[d] *Max Planck Institute of Intelligent Systems, Heisenbergstr. 3, 70569 Stuttgart, Germany*
[e] *Department of Physics, University of California, Merced, CA, 95343, USA*
[f] *Department of Physics and Astronomy, Swarthmore College, Swarthmore, PA, 19081, USA*

† Electronic supplementary information (ESI) available. See DOI: 10.1039/d1sm01209f

knowledge, the literature contains no reports examining director configurations surrounding rod-like particles suspended in LCLCs. Rod asymmetry adds two new degrees of freedom: the aspect ratio (length divided by diameter) of the rod, α, and the mean angle between the long axis of the rod and the uniform far-field director, $\langle\theta\rangle$. These added degrees of freedom create novel possibilities for director configurations with potential consequences for rod orientation and diffusion. Here we employ polarized optical video-microscopy and Landau–de Gennes numerical modeling to elucidate the director configurations around micron sized rods suspended in the aligned nematic phase of a LCLC; we also study the associated angular orientation and diffusion of the rods. Surprisingly, the small twist elastic constant of LCLCs promotes chiral director configurations that modify the natural tendency of rods to orient along the far-field LC alignment axis. Two-thirds of the rods orient at an angle with respect to the uniform far-field director; only one-third have an aligned equilibrium orientation.

These two classes of alignment correspond to two distinct director configurations, both with helical distortions (''twisted tails''), that extend away from the ends of the rods to the far-field director. These director configurations, to the best of our knowledge, have never been reported. Angled rods have identical twisted tails on either end of the rod. However, the handedness of the distortion reverses across a mirror plane located halfway through the diameter of the rod (along the rods long axis and approximately parallel to the confining substrate walls). We call this configuration a ''longitudinal mirror plane'', or ''LMP''. Aligned rods have twisted tails with opposite handedness on either end. Like angled rods, the handedness of the distortion reverses across a longitudinal mirror plane, but unlike angled rods, the handedness of the distortion also reverses across a transverse mirror plane. The transverse mirror plane is perpendicular to the rod's long axis, halfway through the length of the rod. An analogous mirror plane is observed in the Class 2 configuration around spherical particles suspended in aligned LCLCs.[19] We call this configuration surrounding aligned rods a ''transverse and longitudinal mirror plane'', or ''TLMP''.

Note, both LMP and TLMP configurations are globally achiral. Micrographs and schematics of these configurations are shown in Fig. 1–4. Video microscopy reveals that $\langle\theta\rangle$ is inversely correlated with α, and Landau–de Gennes numerical modeling provides strong evidence that the LMP and TLMP configurations are either ground states or deeply metastable states of a LC for which the twist elastic constant (K_2) is significantly less than the splay (K_1) and bend (K_3) elastic constants. Finally, dynamic particle-tracking microscopy confirms that the rods diffuse but are angularly confined, with a confinement strength depending on α. Thus, the rod asymmetry, combined with the exceptionally small twist elastic constant of the LCLC, produce novel spontaneous chiral director configurations that modify the natural tendency of rods to reorient along the LC alignment direction, and induce other interesting behavior. In addition to fundamental insights about the phenomenology, this understanding could be of practical use for mechanical control of rod-like micro- and nanoparticles in LCs.

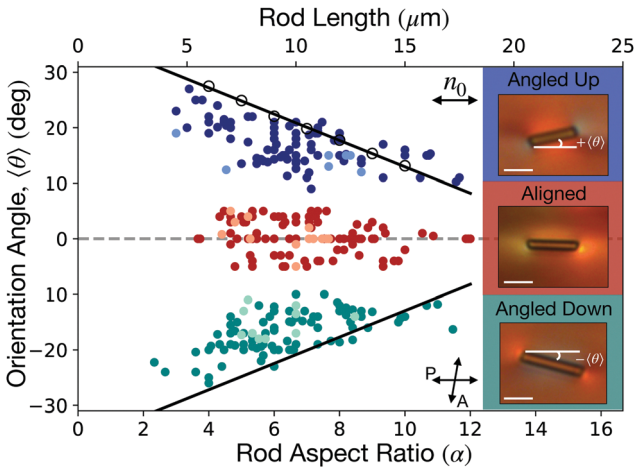

Fig. 1 Dependence of rod orientation angle, $\langle\theta\rangle$, on rod length or aspect ratio, α, in both experiment and simulation. The diameter of all rods is 1.5 μm. The blue, red, and green points correspond to experimental data. The open black circles correspond to simulated rods using LdG modeling. These points are fit to a linear function, shown by the solid black line. A corresponding solid black line for negative $\langle\theta\rangle$ is also provided. The lighter colored points represent rods that appear to have uneven ends (see Section 2.1) as determined by bright field microscopy. The insets show de-crossed analyzer images of the three classes of rods; in these images the blue/red colors indicate the optical rotation induced by the twist deformation. Black arrows show the polarizer (analyzer) at 0° (80°); the far-field director ($\mathbf{n}_0$) is horizontal.

In the remainder of the paper, we describe the experimental video microscopy methods, Landau–de Gennes numerical modeling, and particle-diffusion analyses, and we present our results. The subsequent discussion offers a free energy-based argument for how aligned rods minimize local director

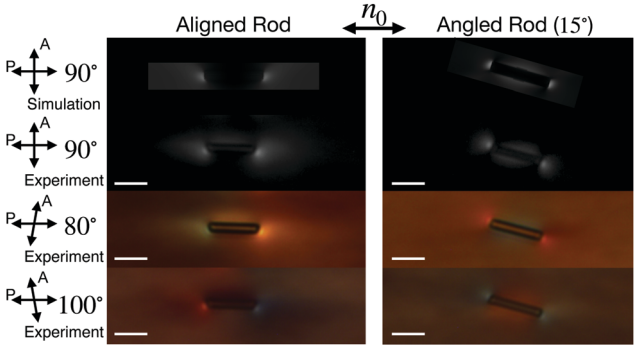

Fig. 2 Simulated and experimental polarized optical micrographs of an aligned rod (left column) and angled rod (right column) in the nematic phase. The top row shows simulated polarized microscopy images. The bottom three rows correspond to experimental images between polarizers with the analyzer at 90° (crossed), 80°, and 100° with respect to input polarizer direction. The uniform far-field director is horizontal. Scale bar (white line) represents 10 μm. With a de-crossed analyzer, the red/blue color indicates the optical rotation induced by the twist deformation. Notice the color of each twisted tail is opposite for aligned rods, and the same for angled rods.

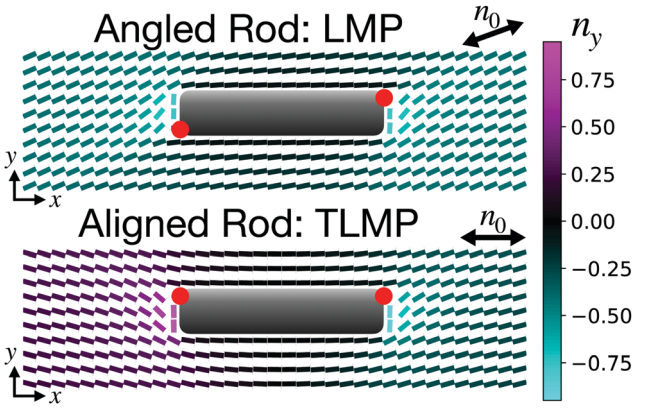

Fig. 3 Simulation results of the director field in a small region around LMP and TLMP rods (grey cylinders), in a slice halfway between and parallel to the confining substrates. Color corresponds to the y component of the director. Red points schematically show the location of defects. Black arrows show orientation of the far-field director $\mathbf{n}_0$.

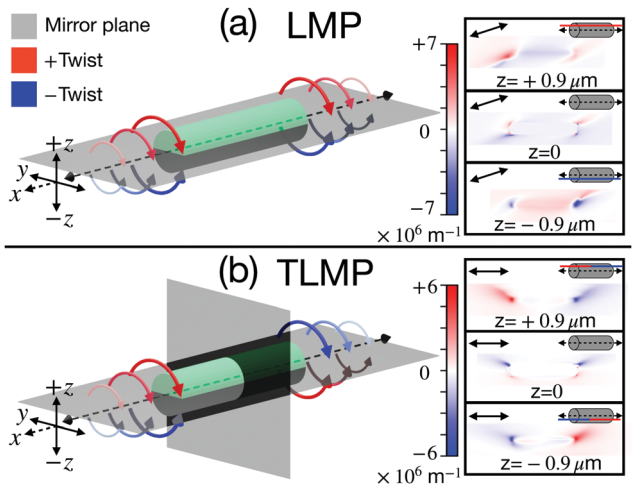

Fig. 4 Schematic of the director field chirality in a longitudinal mirror plane (LMP) director configuration around an angled rod (a), and in a transverse and longitudinal mirror plane (TLMP) director configuration around an aligned rod (b). The gray planes represent mirror planes, across which the handedness of the distortion reverses (as shown by blue and red arrows). The decreasing size and color of the arrows denotes a decreasing magnitude of the twist deformation. The insets show the corresponding twist deformation $\mathbf{n}\cdot(\nabla \times \mathbf{n})$ from numerical director field results for parallel planes above, below, and in the central z = 0 plane. The red/blue color denotes the sign of $\mathbf{n}\cdot(\nabla \times \mathbf{n})$. The upper-right corner of the insets shows the location of these planes schematically, and the orientation of the far-field director $\mathbf{n}_0$ is indicated by a black arrow.

perturbations when both longitudinal and transverse mirror planes are present, and how angled rods minimize local director perturbations when a longitudinal mirror plane is present.

2 Methods

2.1 Experimental preparation and imaging methods

Glass rods (PF-15S, Nippon Electric Glass) are suspended in a lyotropic chromonic liquid crystal made from a 16 wt% solution of disodium cromoglycate (DSCG) in water. The aqueous solution contains 0.015 wt% Triton X100 surfactant to prevent clustering of rods. The chemical structures of DSCG and Triton X100 are shown in Fig. S1 (ESI†). To minimize long-range elastic interactions between rods, the colloid particle number density is chosen such that the inter-rod separation is greater than ten times the average rod length. The concentration of rods in DSCG is 0.05 wt%. When added to water, the plank-like DSCG molecules stack into linear assemblies, and at a high enough concentration, these assemblies order into a nematic phase, in which K_2 is approximately one order of magnitude less than K_1 and K_3.[1] The glass rods have a diameter of (1.49 ± 0.07) μm, and their length distribution is centered at $\sim$9 μm with a standard deviation of $\sim$3 μm.[20] Since the rods are made by breaking a glass fiber, fabrication may leave uneven surfaces on both ends of the rod; thus, these ends are often not flat, not perpendicular to the rod long axis, and not parallel to one another. The shape of the rod ends is determined *via* bright field optical microscopy.

We analyze the orientation of the nematic LC around the rods in planar cells either 12.5 μm or 25 μm thick. The cells are fabricated using two rubbed glass substrates to ensure planar alignment of the LCLC. After filling *via* capillary action, and before imaging, the samples are left to equilibrate for 24 hours ensuring uniform LC alignment. The distance from rod-center to bottom substrate surface was measured by optical microscopy to be approximately 1.5 μm. The equilibrium height of the rod above the substrate is due to a balance between gravitational forces resulting from the density mismatch of glass particles and DSCG solution, and repulsive elastic forces between the substrate and rod caused by director distortions. Imaging is performed using a Leica DM IRB inverted microscope with 100× oil objective (NA = 1.4), an additional 1.6X lens, and a UNIQ UC-1800DS-CL color camera. We image using bright field and polarized optical microscopy (POM), as well as de-crossed analyzer microscopy for which the analyzer is rotated ±10 degrees from its crossed position. Videos are taken at a frame rate of 4–8 fps for a duration of up to 1.5 hours. Only the rods undergoing diffusion (*i.e.*, rods not stuck to the substrate) are chosen for both single frame and video analysis.

2.2 Simulation methods

We use the standard **Q**-tensor based Landau–de Gennes (LdG) numerical model[26,27] to simulate relaxation of a nematic liquid crystal around a rod. This numerical model was also used to simulate the LC configuration around spheres with planar anchoring.[18] The free energy is minimized in a finite difference scheme on a regular cubic mesh using a conjugate gradient algorithm from the ALGLIB package. The open-source version of this code is available online and described in detail in ref. 28. In the uniaxial limit, the LdG free energy is written in terms of the tensor $\mathbf{Q}_{ij} = \frac{3}{2}S\left(\mathbf{n}_i\mathbf{n}_j - \frac{1}{3}\delta_{ij}\right)$, where $\mathbf{n}_i$ is the ith component of the nematic director, δ_{ij} is the Kronecker delta, and S is the nematic order parameter. The nematic director can be recovered from **Q** as the eigenvector corresponding to the largest eigenvalue, S.

The LdG free energy density is the sum of the background phase free energy density and the distortion free energy density:

$$f_{\mathrm{LdG}} = f_{\mathrm{phase}} + f_{\mathrm{d}}. \quad (1)$$

The phase free energy density is:

$$f_{\mathrm{phase}} = \frac{A}{2}\mathrm{Tr}(\mathbf{Q}^2) + \frac{B}{3}\mathrm{Tr}(\mathbf{Q}^3) + \frac{C}{4}(\mathrm{Tr}(\mathbf{Q}^2))^2, \quad (2)$$

where Tr is the trace. We use typical values for LdG parameters of a common nematic liquid crystal, 5CB, $A = (-0.172 \times 10^6)$ J m^{-3}, $B = (-2.12 \times 10^6)$ J m^{-3}, and $C = (1.73 \times 10^6)$ J m^{-3}.[26] The distortion free energy density, using the three-constant approximation, is:

$$f_{\mathrm{d}} = \frac{L_1}{2}\frac{\partial Q_{ij}}{\partial x_k}\frac{\partial Q_{ij}}{\partial x_k} + \frac{L_2}{2}\frac{\partial Q_{ij}}{\partial x_j}\frac{\partial Q_{ik}}{\partial x_k} + \frac{L_3}{2}Q_{ij}\frac{\partial Q_{kl}}{\partial x_i}\frac{\partial Q_{kl}}{\partial x_j}. \quad (3)$$

This is the LdG counterpart to the Frank–Oseen free energy:

$$f_{\mathrm{Frank}} = \frac{K_1}{2}(\nabla \cdot \mathbf{n})^2 + \frac{K_2}{2}(\mathbf{n} \cdot (\nabla \times \mathbf{n}))^2 + \frac{K_3}{2}|\mathbf{n} \times (\nabla \times \mathbf{n})|^2, \quad (4)$$

where K_i are the Frank elastic constants as combinations of L_i.[26] We use reported splay (K_1 = 12 pN), twist (K_2 = 0.8 pN), and bend (K_3 = 27 pN) elastic constants for 16 wt% DSCG.[1] Note that the LdG parameters A, B, and C, are distinct from the elastic constants K_1, K_2, and K_3, with only the latter group adjusted specifically for DSCG in this work.

The boundary free energy is modeled using a Rapini–Papoular surface potential,[29] which is generalized in LdG theory as the Fournier and Galatola form for degenerate planar anchoring.[30] We use degenerate planar anchoring on the rod and substrate surface in order to simulate a small region of aligned nematic surrounding the rod. Because our simulated system is significantly smaller than our experimental system, we use a relatively large anchoring strength of $W = 3 \times 10^{-3}$ J m^{-2}, a value used in similar calculations.[18] Two substrate planes are defined perpendicular to the viewing (z) axis. The other boundary conditions are free, *i.e.*, treated as boundary nodes with zero anchoring potential. The rods are centered in x, y, and z, with their long axis parallel to the substrates. In order to calculate $\langle\theta\rangle$ as a function of α, we fix the orientation of the rod and measure the resulting far-field director orientation. The director field is initialized as a uniform nematic parallel to the substrate walls and long axis of the rod, with a small angular perturbation to prevent the system from becoming fixed in a metastable state. To connect numerical results with experiment, we generate simulated POM images by performing Jones matrix calculations with the computed three-dimensional nematic. The indices of refraction of the 16 wt% DSCG at 650 nm are n_{e} = 1.35 and n_{o} = 1.37.[31,32]

Cylindrical rods are simulated in a box 900 × 150 × 150 units in size, with a mesh size of Δx = 10 nm. The rods are modeled using a ''superegg'' with a diameter of 50 units, a length of 200–500 units, and a sharpness parameter of 10.[27,28] The ''superegg'' is a cylindrical rod with rounded edges; this geometry ensures the occurrence of splay distortion around the edge of the rod. This configuration, with splay distortion, is the most probable, since the experimental rods are very likely rounded on sub-micron scales. In this way, a potential ambiguity in the director field caused by sharp edges is avoided in simulation.[22]

We are not able to observe aligned rods with these simulation parameters, presumably because the simulation finds the lowest energy configuration, and aligned rods are metastable using these simulation parameters. However, by placing small spherical nodes at either end of the rod (with diameters of 12 units), we can pin the defects at the nodes, and obtain a lowest energy configuration that is aligned with the background director. Therefore, while the majority of our numerical results use cylindrical rods, we use the rods with small nodes to visualize the director field around an aligned rod (see Fig. S2, ESI†).

Note, since the system we seek to understand contains defects, the simulation is not entirely scale-free. The defect core size does not scale with system size, which can create discrepancies between numerical results and experimental observations. Furthermore, due to the large aspect ratio of the rods and the maximum simulation size, the diameter of the rods and box are limited to relatively few grid points; as a result, the simulations may be less accurate due to spatial discretization. This limitation increases sensitivity to small perturbations in rod shape. Finally, we use LdG parameters A, B, and C for a thermotropic nematic such as 5CB, rather than DSCG. While this method is common due to the lack of known LdG parameters for LCLCs, it may also introduce discrepancies into our simulation.

2.3 Experimental diffusion and analysis methods

For the diffusion measurements, the center of mass position and instantaneous orientation angle, θ, of rods in each frame of the video are determined using ImageJ with a position resolution of 15 nm and an angular resolution of 0.1°. Systematic drifts in rod motion are estimated using a standard algorithm,[33] and are subtracted prior to analysis. For the translational dynamics, both in the laboratory and body frames, the trajectory data are analyzed following the algorithm described in ref. 34. Of particular importance for the present paper are the angular dynamics. Specifically, we measure the probability distribution of the angle θ relative to the mean orientation angle $\langle\theta\rangle$, and we measure the mean-square angular displacement of this angle, $\langle\Delta\theta^2(t)\rangle$. Note, our approach for measuring translational and rotational diffusion constants of rods is different from the dynamic light scattering method used in ref. 35 and 36.

3 Results

3.1 Experimental results

Initially, the rods are oriented randomly in the isotropic phase of the LCLC. When the sample is cooled into the nematic phase, the rods relax to their equilibrium orientation angle, $\langle\theta\rangle$. Rods angled up are rotated counterclockwise from the far-field director (positive angle), and rods angled down are rotated

clockwise from the far-field director (negative angle). Images of rods in the isotropic and nematic phase are shown in Fig. S3 (ESI†). Measurements of α and $\langle\theta\rangle$ for over 300 rods yield the plot shown in Fig. 1.

Analysis reveals three distinct and stable rod orientations: approximately one third of the rods are angled up, approximately one third are angled down, and approximately one third are parallel to the far-field director. We never observe conversions between angled and aligned rods, nor between positive and negative angled rods. While there is some scatter in the data of Fig. 1, several observations are clearly demonstrated. (1) $\langle\theta\rangle$ decreases as rod length (or α) increases. (2) This relationship between $\langle\theta\rangle$ and α persists, regardless of whether the rod is angled up or down. (3) Rods angled up occur with the same probability as rods angled down. (4) Rod orientation is independent of the shape of the ends of the rod. Specifically, the lighter colored points in Fig. 1 correspond to rods with uneven ends that are either not flat or not perpendicular to the long axis of the rod, or both, as determined *via* bright field optical microscopy (see Section 2.1).

We can further analyze the director field distortion around the aligned and angled rods using polarized optical microscopy, as shown in the inset in Fig. 1, and in more detail in Fig. 2. The bright ends of the rods in the crossed polarized images indicate a local director deformation that differs from the far-field director alignment. Slightly de-crossing the analyzer to either 80° or 100° shows red or blue regions at the rod ends, indicating the sign of the optical rotation due to the twist deformation. Therefore, like colloidal spheres in DSCG,[19] these rods have ''twisted tails'' at their ends. With a de-crossed analyzer, aligned rods have opposite colors at either end, indicating their twisted tails induce optical rotation of the opposite sense. Angled rods have the same color at both ends, indicating their twisted tails induce optical rotation of the same sense. Although all angled rods have identical twisted tails, the induced optical rotation of the twisted tails is reversed for rods angled down compared to rods angled up. Similarly, there is an equal number of aligned rods with red/blue color on the right/left side as there are for the reverse case. A few rods do not relax parallel or at a specific angle to the far-field director, but instead remain roughly perpendicular to the far-field director (see Fig. S4, ESI†). These rods display much larger twisted tails. In addition, some rods chain with other rods either side-by-side or end-to-end (see Fig. S5, ESI†).

3.2 Simulation results

To further understand the configurations of the twisted tails, we perform numerical minimizations of the Landau–de Gennes (LdG) free energy for a nematic director field surrounding a rod. As a validation check, we simulate spheres with parallel anchoring and confirm formation of the same two classes of director configuration reported in ref. 19 (see Fig. S6, ESI†).

We simulate a region of nematic surrounding a cylindrical rod with planar anchoring. The rod is fixed in its orientation, and we obtain $\langle\theta\rangle$ by measuring the resulting angle between the far-field director and the long axis of the rod. Our simulated results for $\langle\theta\rangle$ as a function of α are displayed in Fig. 1 as open black circles. $\langle\theta\rangle$ decreases as α increases, a trend which matches well with experimental data. The simulation also finds the defects of the director field, which are on opposite ends of the rod, diagonal from each other. This defect structure was also observed around cylinders in ref. 22. The defect locations and the local director field surrounding the rod are shown in the upper half of Fig. 3.

Further investigation of the director field reveals configurations different from that of spheres, and to our knowledge, have never been reported. Like the Class 1 configuration for spheres, the twisted tails of angled rods are identical on either end of the rod. However, there is a mirror plane of symmetry halfway through the diameter of the rod across which the handedness of the distortion reverses. This plane contains the long axis of the rod and is approximately parallel to the substrate walls. A schematic of this longitudinal mirror plane (LMP) director configuration is displayed in Fig. 4(a). Flipping the orientation angle, *i.e.*, angled up *versus* angled down, flips the handedness of each tail.

Our simulations show that an angled rod with an LMP director configuration minimizes the free energy of a cylindrical rod suspended in an aligned nematic. However, we still want to understand the director configuration surrounding aligned rods. To this end, we affix small spherical nodes to either end of the rod, thus pinning the defects at each node. This creates a pair of defects on opposite ends of the rod, but along the same edge. The defect locations and surrounding director field are shown in the lower half of Fig. 3. These simulations give $\langle\theta\rangle = 0$ as the lowest energy configuration. The resultant director field has twisted tails with opposite handedness at either end of the rod, reminiscent of the Class 2 configuration of spheres. Since the chirality reverses from one end to the other, there is a mirror plane of symmetry halfway through the length of the rod, perpendicular to the long axis of the rod. In addition, there is also a longitudinal mirror plane along the rod's long axis. A schematic of this transverse and longitudinal mirror plane (TLMP) director configuration is shown in Fig. 4(b). The same configuration with the right- and left-handed regions switched is equally probable.

The twist deformation from numerical director field simulations is shown in the insets of Fig. 4, for both LMP and TLMP configurations. Twist is calculated as $\mathbf{n}\cdot(\nabla \times \mathbf{n})$, where $\mathbf{n}$ is the director field. The twist deformation is shown in the $z = 0$ center plane, parallel to the substrates, as well as in a plane above and below the center plane. Further discussion and visualization of the twisted tail director fields are provided in the ESI† (Fig. S7).

3.3 Diffusion results

Microscopic diffusion measurements of individual tracer particles in a fluid provide information about the transport properties of the fluid and the microenvironment around the particle. In contrast to diffusion of a sphere, diffusion of anisotropic particles can reveal properties of the microenvironment that affect rod translation and rod orientation. Here we present results on rotational diffusion; we discuss the translational diffusion results in the ESI.†

Fig. 5(a) shows exemplary probability distributions of angular fluctuations, $P(\theta - \langle\theta\rangle)$, for two rods ($\alpha$ = 5.9, α = 6.8) about their mean orientation angle $\langle\theta\rangle$. In Table 1, we present best-fit Gaussian functions for the measured probability distributions of five rods with varying α and $\langle\theta\rangle$. The standard deviations of these distributions are less than 0.3°, suggesting strong angular confinement of the rods about their mean orientations. As evident from Table 1, the angular standard deviation σ_θ, which reflects the strength of the angular confining potential, depends inversely on α, but does not depend on $\langle\theta\rangle$. Interestingly, the angular confining potential is about the same for aligned *versus* angled rods (within systematic and random errors).

Fig. 5(b) displays the angular mean-squared displacement $\langle\Delta\theta^2(t)\rangle$ for two rods with distinct α. For free angular diffusion of a rod, we would expect $\langle\Delta\theta^2(t)\rangle \sim t$. However, for these rods, $\langle\Delta\theta^2(t)\rangle \sim t^\nu$ with $\nu < 1$. This observation (and others) indicates sub-diffusive behavior of an orientationally trapped particle in an angular potential well. Irrespective of α, the sub-diffusive exponent ν is observed to be largest at short lag time ($t < 2$ s), decreasing during intermediate times (2 s $< t <$ 10 s), and finally saturating to $\nu \approx 0$ at long times ($t >$ 100 s). Such dynamic behavior is reminiscent of the orientational trapping of anisotropic particles by their neighbors in dense packings of ellipsoids called orientational glasses.[37,38] As was the case for our observations of the standard deviation of the angular probability distribution (σ_θ), which trended inversely with increasing α, we find that the $\langle\Delta\theta^2(t)\rangle$ of rods with higher α tend to saturate at lower values compared to rods with smaller α.

We can estimate an angular elastic coefficient, κ_θ, for each rod by fitting a Gaussian function to the angular distribution of θ (Table 1). For small angular fluctuations about $\langle\theta\rangle$, the distribution can be expressed as:

$$P(\phi) \sim e^{-\kappa_\theta \phi^2/k_B T}, \quad (5)$$

where $\phi = \theta - \langle\theta\rangle$, and $k_B T$ is the thermal energy.[39–41] In order to compare the experimentally estimated angular elastic coefficients to theoretical models, we use the expression for κ_θ derived for a cylindrical particle in a nematic liquid crystal:[42]

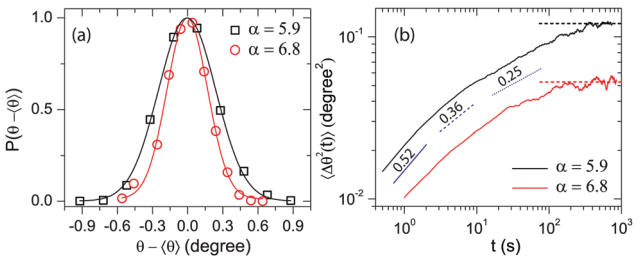

Fig. 5 (a) Probability distribution of angular fluctuations of the rod, $P(\theta - \langle\theta\rangle)$, for two rods of different aspect ratio, α. The distributions for both rods peak at $(\theta - \langle\theta\rangle) \sim 0$. The probability axis has been scaled such that $P(\theta - \langle\theta\rangle) = 1$ at $(\theta - \langle\theta\rangle) = 0$. Solid lines are Gaussian fits to the data. (b) Angular mean-squared displacement $\langle\Delta\theta^2(t)\rangle$ for the two rods whose distributions are shown in (a). The solid, dashed, and dotted blue line segments have slopes of 0.52, 0.36 and 0.25, respectively. The horizontal dashed lines indicate the saturation value of $\langle\Delta\theta^2(t)\rangle$.

Table 1 Angular diffusion behavior. α is the aspect ratio of the rod, $\langle\theta\rangle$ is the mean angle between the long axis of the rod and the uniform far-field director, σ_θ is the standard deviation of the angular probability distribution, $\langle\Delta\theta^2(t)\rangle_{sat}$ is the saturation value of the angular MSD, and κ_θ is the deduced angular elastic constant

α	$\langle\theta\rangle$ (degrees)	σ_θ (degrees)	$\langle\Delta\theta^2(t)\rangle_{sat}$ (degrees^2)	$\kappa_\theta \times 10^4 k_B T$
4.6	13.7	0.25 ± 0.005	0.09 ± 0.01	2.63 ± 0.11
5.9	0.7	0.28 ± 0.005	0.18 ± 0.02	2.09 ± 0.07
5.9	−15.0	0.24 ± 0.005	0.12 ± 0.01	2.85 ± 0.12
6.8	−17.8	0.17 ± 0.005	0.05 ± 0.01	5.68 ± 0.32
6.9	−12.5	0.15 ± 0.005	0.04 ± 0.01	7.29 ± 0.46

$$\kappa_{theory} = 2\pi CK. \quad (6)$$

Here, K is the average LC Frank elastic constant, and C is a geometric factor of the cylindrical particle given by:

$$C = \frac{2L\beta}{\ln\left(\frac{1+\beta}{1-\beta}\right)}, \quad \text{where } \beta = \sqrt{1 - \left(1 - \frac{1}{\alpha^2}\right)}, \quad (7)$$

and L is the rod length. When α = 6 and $K \sim$ 13.2 pN for 16 wt% DSCG,[1] then $\kappa_{theory} \sim 7.22 \times 10^4 k_B T$; this theoretical estimate is the same order of magnitude as the experimentally determined κ_θ reported in Table 1.

4 Discussion

4.1 Simple free energy model

If one assumes the director configuration around a rod in a LCLC is qualitatively similar to that of a sphere, then some simple arguments explain the observed behavior. Spheres and rods with tangential anchoring cause the director to distort near the object in regions where the background director is not parallel to the object surface. Due to the small twist elastic constant of LCLCs (*i.e.*, relative to the other elastic constants), this director distortion results in "twisted tails" around the ends of spheres and rods.

Fig. 6 shows schematics of director lines surrounding a rod for four different configurations. The director lines are based on the equation for a helix, and they are manipulated such that the director field surrounding the rod has the symmetry required by the TLMP and LMP configurations. These equations are given in the ESI.† The mean angle between the rod's long axis and the uniform far-field director is $\langle\theta\rangle$, and the angle between the local director and the far-field director at each point along the director field line is β. For clarity, only two director lines are shown on the helical (Helix) and LMP rods; thus, one must imagine a family of similar director lines wrapping about the curved surface of the rod. Since the shapes of the director lines of a TLMP configuration vary for different points on the rods surface, multiple director lines are shown. The simplest nontrivial configuration is a helical director field; in this case, the twisted tails have the same handedness on either side and there is an overall chirality (*i.e.*, like the Class 1 configuration for spheres). If a longitudinal mirror plane is present, the director lines on either side look identical when viewed along a direction

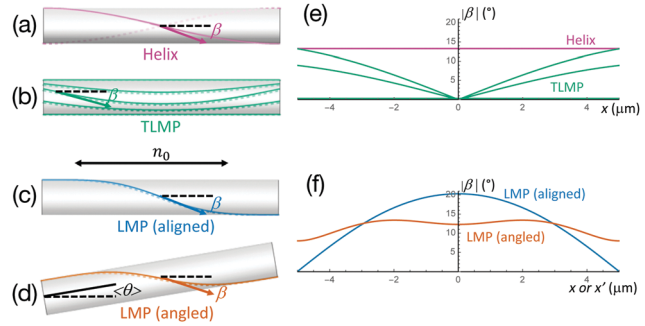

Fig. 6 Schematics of four possible director configurations around rods with tangential anchoring: (a) helical (Helix), (b) transverse and longitudinal mirror plane (TLMP), (c) longitudinal mirror plane (LMP) around an aligned rod, and (d) LMP around an angled rod. Mathematical expressions for the director field equations are given in the ESI.† Solid and dashed lines indicate the director just above and just below the rod, respectively. Since they are "reflections" of each other when an LMP is present, the view has been slightly offset to show both. Note that the director has an out-of-plane component not pictured in these schematics (illustrated in more detail in Fig. S8, ESI†). The far-field director $\mathbf{n}_0$ is horizontal. $\langle\theta\rangle$ is the mean angle between the long axis of the rod and the uniform far-field director, and β is the angle between the local director and the far-field director at each point along the director field line. The corresponding plots in (e) and (f) show $|\beta|$ along the long axis of the rod (along x for aligned rods, along x' for angled rods). The TLMP configuration has two pairs of symmetric director lines. Their $|\beta|$ *vs.* x plots overlap and only three TLMP lines are visible in (e).

perpendicular to the mirror plane. This LMP configuration is illustrated for both an aligned and angled rod in Fig. 6. If the two twisted tails have opposite handedness on the same side of the LMP, a transverse mirror plane must be present in the middle of the rod. Such a TLMP configuration with both transverse and longitudinal mirror planes is shown. For 3D schematics of these director fields, see Fig. S8 (ESI†). Fig. 6 also shows $|\beta|$ along the long axis of the rod. Notice that a TLMP configuration minimizes the average value of $|\beta|$ compared to a helix, and an angled rod minimizes the average value of $|\beta|$ for an LMP configuration.

Utilizing the fact that any deviation of the director field from the uniform far-field director will cost energy, we construct a simple calculation to predict $\langle\theta\rangle$, which assigns an angle-dependent energy cost between local and far-field director fields. The details of this calculation are discussed in the ESI,† wherein equations for the three possible director configurations of Fig. 6 are generated mathematically. We calculate β at all points along the director line for each configuration and at varying $\langle\theta\rangle$. We approximate the free energy to be proportional to $\langle\sin^2\beta\rangle$, a simple relationship reminiscent of anchoring potentials.[29] When the director on the rod surface aligns more with the far-field director, $\langle\sin^2\beta\rangle$ becomes smaller.

Results are shown in Fig. 7(a). For the helical and TLMP configurations, $\langle\sin^2\beta\rangle$ is minimized when $\langle\theta\rangle = 0$. Furthermore, at $\langle\theta\rangle = 0$, $\langle\sin^2\beta\rangle$ is lowest for the TLMP configuration. This offers an explanation as to why we only observe TLMP configurations around aligned rods: it minimizes the free energy. For the LMP configuration, the minimum value of $\langle\sin^2\beta\rangle$ occurs for a non-zero $\langle\theta\rangle$. We calculate the free energy $\langle\sin^2\beta\rangle$ for various aspect ratios with this configuration and find that $\langle\theta\rangle$ increases as α decreases. These results are shown in Fig. 7(b). They are consistent with the trend observed experimentally and numerically in Fig. 1.

4.2 Discussion of experimental and simulation results

Our experimental and simulated data together exhibit a strong correlation between $\langle\theta\rangle$ and α, as shown in Fig. 1. Diffusion results also suggest that angular confinement increases in strength with larger α.

The de-crossed analyzer experimental data and simulation results support each other. Simulations reveal that the LMP configuration has identical twisted tails on either end, consistent with the observation in Fig. 2 that angled rods viewed with a de-crossed analyzer have tails of the same color. Similarly, the TLMP configuration has twisted tails of opposite handedness on either end of the rod, consistent with the observation in Fig. 2 that aligned rods viewed with a de-crossed analyzer have opposite tail colors.

Numerical simulations show that an angled configuration minimizes the free energy over an aligned configuration for a cylindrical rod with planar anchoring. However, it is important to note that the simulation differs from experiment in significant ways, including overall scale, defect core size, and LdG parameters (A, B, and C), all of which could affect the final director field configuration.

Finally, microscopy reveals that the glass rods used in experiment often have rough or uneven faces due to the method of fabrication (see Section 2.1). These edges could act as pinning sites for defects in the director field, leading to the two different defect patterns shown in Fig. 3, and consequently, the two different director configurations. Further experimental investigation is necessary to disentangle and understand this effect.

4.3 Discussion of diffusion results

The diffusion analysis reveals that the rods are orientationally trapped in a strong angular potential well, *i.e.*, a well with a free energy barrier preventing significant changes in $\langle\theta\rangle$. Consequently, the rods show only small angular fluctuations about their mean orientation, irrespective of the angle of alignment relative to the far-field director. Interestingly, while previous studies report a relatively easier orientational motion of the aligned rods (compared to rods

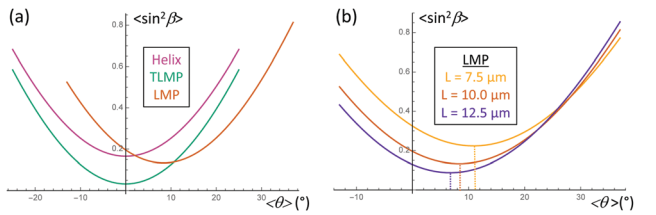

Fig. 7 (a) Dependence of $\langle\sin^2\beta\rangle$ on the angle $\langle\theta\rangle$ between the long axis of the rod and the far field director for the three model director configurations with radius r = 0.75 μm and length L = 10 μm. (b) Dependence of $\langle\sin^2\beta\rangle$ on $\langle\theta\rangle$ for the LMP director configuration for three different rod lengths (r = 0.75 μm) and aspect ratios. The minimum of each curve is indicated with vertical dashed lines.

at $\langle\theta\rangle = 90^\circ$),[41] the trends we find suggest that the strength of angular confinement depends primarily on α. To our knowledge, the alignment and resultant diffusion of rods at small finite angle ($\langle\theta\rangle \neq 0^\circ$) with respect to the far-field director axis have not been reported. In these situations, orientational motion can strongly couple with translational motion and can influence the translation diffusion. Here, in a limited data set, translational diffusion is found to be anisotropic along different axes, and its anisotropy is more pronounced for the aligned rod compared to the angled one. The translational diffusion data are tabulated and discussed in the ESI.†

5 Conclusions

Rod-like particles suspended in LCLCs generate a landscape of rich behaviors with a multitude of mirror symmetry breaking phenomena. Contrary to expectations, we discover that rods in a LCLC often prefer an angled orientation with respect to the far-field director. This behavior originates from the inherent asymmetry of rods and the relatively small twist elastic constant of LCLCs. Since twist distortions are energetically cheap, twisted tails form on either side of the rod, leading to two distinct director configurations associated with the two different equilibrium orientation states. Angled rods show an LMP configuration, while aligned rods show a TLMP configuration, both never before observed. We have elucidated the details of these configurations schematically, experimentally, and through numerical modeling. Furthermore, we observe that the preferential orientation angle of LMP rods is inversely related to their aspect ratio. Angular diffusion analysis supports these findings; the rods are orientationally trapped in an angular potential well, and the strength of the confinement increases with aspect ratio. Our study highlights the importance of twist effects in determining director orientations in a LCLC. A deeper understanding of the coupling between twist distortions in LCLCs and the orientation of suspended colloids could also be of practical use, because it offers new concepts for controlling anisotropic micro- and nano-particles in LCs and for assembling complex particle structures in LCs. Design and control of the chiral tails creates potential for spinning and/or propelling particles in a LCLC, which could be useful for colloid-based active matter.

Conflicts of interest

There are no conflicts to declare.

Acknowledgements

This work was supported by the NSF (DMR2003659), the PENN MRSEC (DMR1720530) including its Optical Microscopy Shared Experimental Facility, and the NASA (80NSSC19K0348). The authors thank I. Musevic for providing the glass rods, A. de la Cotte and F. Sterl for experimental assistance, A. Martinez and R. D. Kamien for useful discussions, and M. Tanaka for assistance with figures.

Notes and references

1 S. Zhou, K. Neupane, Y. A. Nastishin, A. R. Baldwin, S. V. Shiyanovskii, O. D. Lavrentovich and S. Sprunt, *Soft Matter*, 2014, **10**, 6571–6581.
2 P. P. Karat and N. V. Madhusudana, *Mol. Cryst. Liq. Cryst.*, 1977, **40**, 239–245.
3 J. Bunning, T. Faber and P. Sherrell, *J. Phys.*, 1981, **42**, 1175–1182.
4 T. Toyooka, G.-p. Chen, H. Takezoe and A. Fukuda, *Jpn. J. Appl. Phys.*, 1987, **26**, 1959–1966.
5 H. Stark, *Phys. Rep.*, 2001, **351**, 387–474.
6 O. D. Lavrentovich and E. M. Terentjev, *J. Exp. Theor. Phys.*, 1986, **64**, 1237.
7 P. S. Drzaic, *Liq. Cryst.*, 1999, **26**, 623–627.
8 A. Rudinger and H. Stark, *Liq. Cryst.*, 1999, **26**, 753–758.
9 P. W. Ellis, K. Nayani, J. P. McInerney, D. Z. Rocklin, J. O. Park, M. Srinivasarao, E. A. Matsumoto and A. Fernandez-Nieves, *Phys. Rev. Lett.*, 2018, **121**, 247803.
10 J. Jeong, Z. S. Davidson, P. J. Collings, T. C. Lubensky and A. G. Yodh, *Proc. Natl. Acad. Sci. U. S. A.*, 2014, **111**, 1742–1747.
11 J. Jeong, L. Kang, Z. S. Davidson, P. J. Collings, T. C. Lubensky and A. G. Yodh, *Proc. Natl. Acad. Sci. U. S. A.*, 2015, **112**, E1837–E1844.
12 Z. S. Davidson, L. Kang, J. Jeong, T. Still, P. J. Collings, T. C. Lubensky and A. G. Yodh, *Phys. Rev. E: Stat., Nonlinear, Soft Matter Phys.*, 2015, **91**, 050501.
13 K. Nayani, R. Chang, J. Fu, P. W. Ellis, A. Fernandez-Nieves, J. O. Park and M. Srinivasarao, *Nat. Commun.*, 2015, **6**, 8067.
14 C. F. Dietrich, P. Rudquist, K. Lorenz and F. Giesselmann, *Langmuir*, 2017, **33**, 5852–5862.
15 C. F. Dietrich, P. Rudquist, P. J. Collings and F. Giesselmann, *Langmuir*, 2021, **37**, 2749–2758.
16 L. Tortora and O. D. Lavrentovich, *Proc. Natl. Acad. Sci. U. S. A.*, 2011, **108**, 5163–5168.
17 K. Nayani, J. Fu, R. Chang, J. O. Park and M. Srinivasarao, *Proc. Natl. Acad. Sci. U. S. A.*, 2017, **114**, 3826–3831.
18 A. Nych, U. Ognysta, I. Muševič, D. Seč, M. Ravnik and S. Žumer, *Phys. Rev. E: Stat., Nonlinear, Soft Matter Phys.*, 2014, **89**, 062502.
19 A. Martinez, P. J. Collings and A. G. Yodh, *Phys. Rev. Lett.*, 2018, **121**, 177801.
20 U. Tkalec, M. Škarabot and I. Muševič, *Soft Matter*, 2008, **4**, 2402.
21 M. Tasinkevych, F. Mondiot, O. Mondain-Monval and J.-C. Loudet, *Soft Matter*, 2014, **10**, 2047.
22 D. A. Beller, M. A. Gharbi and I. B. Liu, *Soft Matter*, 2015, **11**, 1078–1086.
23 M. R. M, R. K. Pujala and S. Dhara, *Sci. Rep.*, 2019, **9**, 4652.
24 F. Brochard and P. de Gennes, *J. Phys.*, 1970, **31**, 691–708.
25 S. V. Burylov and Y. L. Raikher, *Phys. Rev. E: Stat. Phys., Plasmas, Fluids, Relat. Interdiscip. Top.*, 1994, **50**, 358–367.
26 M. Ravnik and S. Žumer, *Liq. Cryst.*, 2009, **36**, 1201–1214.
27 D. A. Beller, PhD Thesis, University of Pennsylvania, 2014.
28 D. M. Sussman and D. A. Beller, *Front. Phys.*, 2019, **7**, 204.

29 A. Rapini and M. Papoular, *J. Phys. Colloques*, 1969, **30**, C4-54–C4-56.
30 J.-B. Fournier and P. Galatola, *Europhys. Lett.*, 2005, **72**, 403–409.
31 Y. A. Nastishin, H. Liu, T. Schneider, V. Nazarenko, R. Vasyuta, S. V. Shiyanovskii and O. D. Lavrentovich, *Phys. Rev. E: Stat., Nonlinear, Soft Matter Phys.*, 2005, **72**, 041711.
32 P. C. Mushenheim and N. L. Abbott, *Soft Matter*, 2014, **10**, 8627–8634.
33 J. C. Crocker and D. G. Grier, *J. Colloid Interface Sci.*, 1996, **179**, 298–310.
34 Y. Han, A. M. Alsayed, M. Nobili, J. Zhang, T. C. Lubensky and A. G. Yodh, *Science*, 2006, **314**, 626–630.
35 R. Nixon-Luke and G. Bryant, *Part. Part. Syst. Charact.*, 2019, **36**, 1800388.
36 D. Feller, M. Otten, M. Hildebrandt, M. Krüsmann, G. Bryant and M. Karg, *Soft Matter*, 2021, **17**, 4019–4026.
37 C. K. Mishra, A. Rangarajan and R. Ganapathy, *Phys. Rev. Lett.*, 2013, **110**, 188301.
38 C. K. Mishra, K. Hima Nagamanasa, R. Ganapathy, A. K. Sood and S. Gokhale, *Proc. Natl. Acad. Sci. U. S. A.*, 2014, **111**, 15362–15367.
39 P. G. d. Gennes and J. Prost, *The Physics of Liquid Crystals*, Clarendon Press, 1993.
40 P. M. Chaikin and T. C. Lubensky, *Principles of Condensed Matter Physics*, Cambridge University Press, Cambridge, 1995.
41 B. Senyuk, D. Glugla and I. I. Smalyukh, *Phys. Rev. E: Stat., Nonlinear, Soft Matter Phys.*, 2013, **88**, 062507.
42 C. J. Smith and C. Denniston, *J. Appl. Phys.*, 2007, **101**, 014305.